Journal of Alloys and Compounds 1051 (2026) 186026

Contents lists available at ScienceDirect

Journal of Alloys and Compounds

journal homepage: www.elsevier.com/locate/jalcom

MXene-assisted interface engineering for strengthening aluminium matrix composites via high-pressure torsion

Jing Ye [a], Abdelrahman Elsayed [b,d], Tarek Allam [c,d], Walaa Abd-Elaziem [e,f], Ali Reza Kamali [g], Amr M. Abdelkader [a,*], Yi Huang [a,*]

[a] School of Computing and Engineering, Faculty of Media, Science and Technology, Bournemouth University, Poole BH12 5BB, UK
[b] Steel Institute, RWTH Aachen University, Aachen 52072, Germany
[c] Institute of Energy Materials and Devices, Structure and Function of Materials (IMD-1), Forschungszentrum Jülich GmbH, Jülich 52425, Germany
[d] Department of Metallurgical and Materials Engineering, Suez University, Suez, 43528, Egypt
[e] Department of Mechanical Design and Production Engineering, Faculty of Engineering, Zagazig University, P.O. Box 44519, Egypt
[f] Department of Materials Science and Engineering, Northwestern University, Evanston, IL 60208, USA
[g] Energy and Environmental Materials Research Centre (E2MC), School of Metallurgy, Northeastern University, Shenyang 110819, China

ARTICLE INFO

Keywords:
Aluminium matrix composites
MXene
High-pressure torsion
Electrostatic self-assembly strategy
Mechanical property

ABSTRACT

Owing to its intrinsic two-dimensional structure, combined with its functionalized surfaces and superior mechanical properties, $Ti_3C_2T_x$ (MXene) has emerged as a highly attractive candidate for reinforcing aluminium matrix composites (AMCs) in advanced structural applications. In this study, few-layer MXene (FMXene) was successfully incorporated into pure aluminium via an electrostatic self-assembly strategy followed by high-pressure torsion (HPT) processing at room temperature. The microstructure evolution of FMXene-Al composites was systematically investigated, revealing that this integrated processing strategy effectively induced grain refinement and facilitated the homogeneous dispersion of FMXene. The microhardness of the FMXene-Al composites increased with both the number of HPT turns and the FMXene content (wt%), reaching a maximum value of approximately 140 HV. Notably, a favourable trade-off between strength and ductility was achieved at an FMXene content of 0.5 wt%, where the ultimate tensile strength (UTS) reached 290 MPa while retaining appreciable ductility of ~ 1 %. This work provides valuable insights into the development of nanostructured, high-performance AMCs via room temperature, interface-engineered processing routes.

1. Introduction

Since their introduction in the early 20 century, aluminium-matrix composites (AMCs) have undergone significant development, driven by the increasing demand for lightweight, high-performance materials in transportation and aerospace sectors [1–3]. The unique combination of low density, high strength, and decent ductility renders AMCs highly attractive for applications from consumer electronics to automotive and aerospace, enabling reduced fuel consumption without compromising structural integrity [4,5]. Over decades of research, efforts to enhance the properties of AMCs have largely focused on the incorporation of reinforcing phases. While ceramic reinforcements like SiC and Al_2O_3 offer excellent mechanical properties, their intrinsic brittleness and poor machinability have limited their widespread adoption. Similarly, metal oxides, despite their compatibility with aluminium, often fail to achieve the desired balance of strength and ductility [6,7]. Carbon-based materials, particularly graphene, have long been considered an ideal reinforcement material due to their remarkable properties [8]. However, challenges such as agglomeration and poor interfacial wettability between graphene and aluminium have significantly hindered its practical viability in AMCs, despite its theoretical advantages [9–12]. In this context, MXene has emerged as a promising alternative, combining the benefits of carbon-based materials with improved compatibility, stability, and enhanced wettability with the aluminium matrix. MXene as a two-dimensional material, exhibits excellent electrical conductivity and remarkable mechanical properties, with an electrical conductivity of 11000 S cm^{-1}, Young's modulus reaching up to 500 GPa and tensile strength up to 15.4 GPa, making it an attractive candidate for reinforcing AMCs [13–17]. In comparison to graphene, MXene shows improved dispersion stability, owing to its abundant surface functional

* Corresponding authors.
E-mail addresses: aabdelkader@bournemouth.ac.uk (A.M. Abdelkader), yhuang2@bournemouth.ac.uk (Y. Huang).

https://doi.org/10.1016/j.jallcom.2026.186026
Received 9 November 2025; Received in revised form 23 December 2025; Accepted 5 January 2026
Available online 6 January 2026

groups (-OH, -COOH), these functional groups can generate electrostatic repulsion in dispersion and chemical affinity with the aluminium matrix, which not only mitigate agglomeration but also enhance wetting ability with aluminium [18–22]. Those improvements underscore the potential of MXene as an effective reinforcement in AMCs.

One major challenge associated with carbon-based reinforcement in AMCs is the formation of the needle-shaped Al_4C_3 phase at temperatures exceeding 600 ℃ during conventional high-temperature processing techniques such as selective laser melting, stir casting, and friction stir welding [9,23–25]. This brittle Al_4C_3 phase significantly degrades the composite's mechanical properties and compromises its structural integrity [26–28]. To address this issue, strategies that prevent Al_4C_3 formation are essential for achieving high-performance AMCs. High-pressure torsion (HPT), a severe plastic deformation (SPD) technique, offers a viable solution by enabling composite processing at room temperature [29]. By eliminating the risk of Al_4C_3 formation, HPT ensures that the reinforcing phase retains its structural and functional properties. Additionally, the intense shear strain and elevated pressure applied during HPT facilitate significant grain refinement and the uniform dispersion of reinforcing phases, further enhancing the composite's mechanical properties without inducing phase transformations or structural degradation [30–32].

The integration of MXene as a reinforcement and the application of HPT as a forming technique presents a transformative approach for addressing longstanding challenges in AMCs development. By combining the exceptional properties of MXene with the advanced processing capabilities of HPT, this strategy offers a pathway to develop lightweight, high-performance materials for structural and functional applications. This study focuses on investigating the strengthening mechanism of MXene within the aluminium matrix by employing MXene reinforcements with different morphologies and layer structures, and on optimizing the interface design to achieve both high performance and improved economic efficiency in AMCs.

2. Experimental section

2.1. Materials and preparations

The matrix material, aluminium powder (99.5 % purity, maximum particle size of 125 μm) was obtained from Goodfellow. The MXene colloid was synthesized in the lab by etching aluminium from Ti_3AlC_2 (MAX) phase using in-situ generation hydrofluoric acid (HF). Fig. 1 is a schematic diagram showing the steps of preparation of MXene-Al composites. Further details of each step will be demonstrated in the following sections.

2.1.1. Few-layer MXene preparation

In a polytetrafluoroethylene (PTFE) conical flask, 3.2 g of LiF was dissolved in 40 mL of 9 mol L^{-1} HCl and kept at 45 °C for 15 min to ensure sufficient dissolution and in-situ generation of HF. Subsequently, 2 g of Ti_3AlC_2 was slowly added, and the etching was carried out at 45 ℃ with a stirring speed of 500 rpm for 48 h, during which the aluminium layers were selectively removed from Ti_3AlC_2 phase. After completion of the reaction, the obtained product was transferred to a centrifuge tube and centrifuged at 3500 rpm for 5 min, this process was repeated 7–8 times until the solution reached a PH of 6. The resulting product multilayer MXene (named as MMXene) was then mixed with deionized water and transferred to an air washing setup. The equipment was placed in an ultrasonic bath filled with ice water and sonicated for one hour under an argon atmosphere. After ultrasonication, the liquid was poured into a centrifuge tube and centrifuged at 3500 rpm for 30 min. The resulting supernatant, which contains few-layer MXene solution, is hereafter referred to as FMXene.

2.1.2. FMXene-Al powder mixture preparation by electrostatic self-assembly

To prepare the FMXene-Al powder mixture, aluminium powder was slowly introduced into the FMXene colloidal solution under continuous stirring at its naturally established PH (~ 6). The suspension was then stirred vigorously for 30 min to facilitate electrostatic self-assembly and ensure homogeneous mixing. After self-assembly, the suspension was vacuum filtrated and dried to obtain FMXene-Al composite powders containing 0.5 wt%, 1 wt%, and 5 wt% FMXene. For instance, "0.5FMXene-Al" refers to a composite containing 0.5 wt% FMXene in the aluminium matrix. The concentration of the FMXene colloidal solution used for preparation was determined by vacuum-filtration and freeze-drying (see Supporting Information for details). For comparison, MMXene-Al composites with 5 wt% MMXene (referred to as "5MMXene-

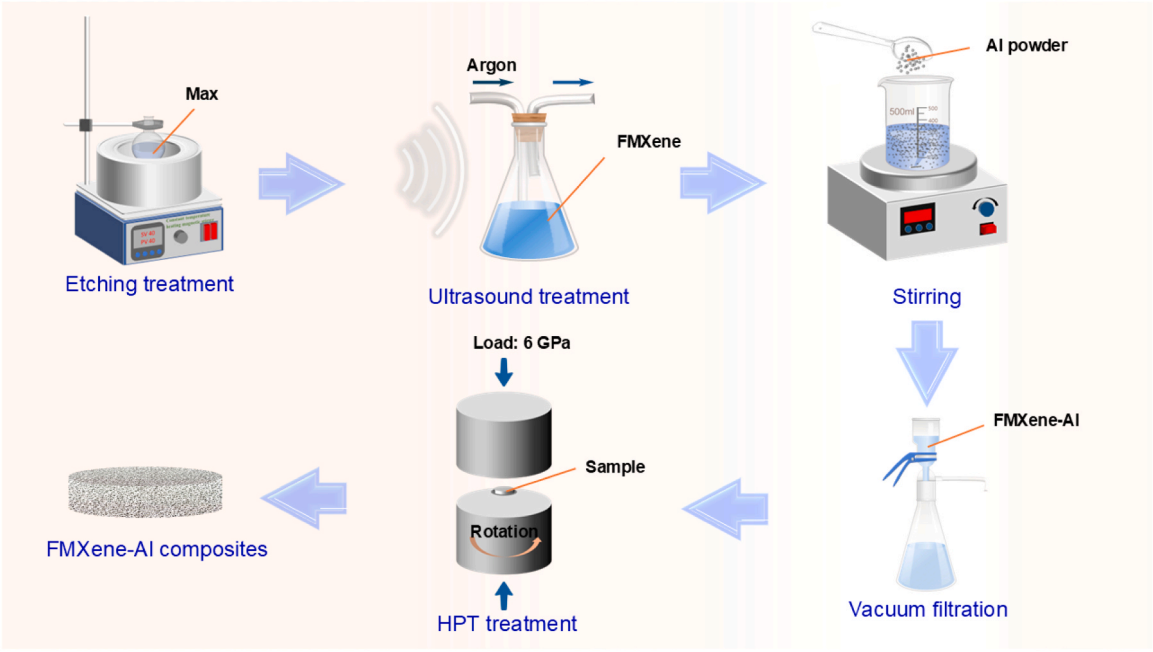

Fig. 1. Schematic diagram of preparation of FMXene-Al composites.

Al") was prepared following the same procedure as that used for the FMXene-Al samples.

2.1.3. FMXene-Al composites fabricated by HPT process

0.2 g of FMXene-Al mixture powder was cold-pressed in a cylindrical mold under manual load for half a minute. The obtained green compacts, with 10 mm in diameter and 0.85 mm in height, were then subjected to HPT processing at room temperature. This involved applying a pressure of 6.0 GPa with an anvil rotation speed set at 1 rpm, and green samples were processed to 0, 1, 5, and 20 turns (denoted as 0 N, 1 N, 5 N, and 20 N).The 0 N sample was used as a reference to show the influence of shear strain induced by HPT on the microstructure evolution. It should be noted that the entire HPT process was carried out under quasi-constrained conditions, where friction between the sample and anvils restricted radial flow, allowing only a small amount of material flowing out around the edge of sample, therefore, the total weight of the final sample is approximately 0.17 g.

2.2. Characterization methods

All the samples were polished using abrasive paper of 1200#, 3000# and then polished with diamond paste at a size of 0.1 μm. The phase composition of all samples was examined using X-ray diffraction (XRD) with Kα radiation (Siemens, Germany). Surface morphology and microstructural features were analysed using a Zeiss Sigma field emission gun scanning electron microscope (FEG-SEM, Carl Zeiss Microscopy GmbH, Jena, Germany), equipped with secondary-electron imaging (SE) and electron backscatter diffraction (EBSD) detectors. EBSD maps were acquired with a step size of 60 nm. The dispersion and interfacial bonding state of the FMXene-Al composites were observed by transmission electron microscopy (TEM, JEOL JEM-2100) coupled with energy-dispersive spectroscopy (EDS). The chemical states of the samples were characterized using X-ray photoelectron spectroscopy (XPS, Kratos AXIS Supra). Microhardness was measured using a Vickers hardness tester (Buehler VH1102, Germany) under a load of 200 g and a dwell time of 15 s. Tensile testing was performed at room temperature using a Zwick testing machine (Zwick/Roell Z030, Germany). Miniature tensile specimens were extracted from the HPT-processed disc using wire electrical discharge machining (wire EDM), yielding two samples with approximate dimensions of 2 mm in gauge length, 1 mm in width, and 0.6 mm in thickness. The drawing of specific cutting position and dimension is shown in Fig. S1 (Supporting Information). During tensile tests, the displacement rate was held constant, and the initial strain rate was maintained at $1 \times 10^{-3}\ s^{-1}$. Engineering strain was calculated from the crosshead displacement. Due to the small gauge length of the miniature specimens and the influence of machine and grip compliance, the initial elastic portion of the stress-strain curves does not represent the true Young's modulus of the material. Therefore, elongation was evaluated as the plastic strain to fracture by subtracting the initial 0.2 % strain.

3. Results and discussion

3.1. Interfacial interaction mechanism between FMXene and aluminium

Fig. 2 presents a schematic illustrating the mechanism for the formation of FMXene-Al composite powders through a facile self-assembly process conducted under weaky acidic conditions (PH ≈ 6). Specifically, aluminium rapidly forms a dense and stable oxide layer (Al_2O_3) upon exposure to ambient air due to its high reactivity with oxygen.

When in contact with water, this oxide layer undergoes hydrolysis, generating hydroxyl (-OH) groups on its surface. Furthermore, under the weakly acidic environment, partial dissolution and protonation of the alumina layer occur, leading to the formation of locally active Al-OH_2^+ sites and exposing fresh metallic areas [33–35]. This mild surface activation generates abundant reactive hydroxyl groups and positively

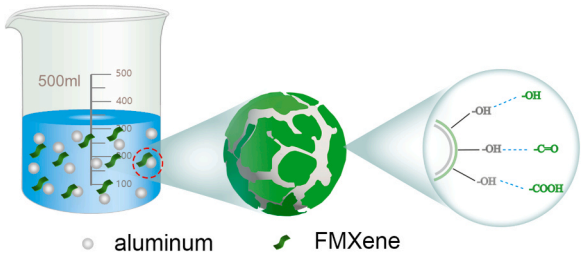

Fig. 2. Schematic illustration of the formation mechanism of FMXene-Al powder.

polarized sites on the aluminium surface. Simultaneously, FMXene nanosheets possess negatively charged surface terminations such as -O, -OH, and -COOH, which can readily interact with these sites [16,17]. The hydrogen bonding and localized electrostatic attractions between FMXene functional groups and the hydroxylated aluminium surface drive the spontaneous self-assembly of FMXene sheets onto the surface of aluminium particles, forming a conformal and uniform coating. This interfacial process, governed by interfacial physicochemical interactions between both materials, resulting in strong adhesion and homogeneous coverage of the FMXene nanosheets, thereby forming a stable FMXene-Al composite structure.

To validate this self-assembly mechanism, various characterization techniques were employed. The morphology of MMXene, FMXene, aluminium and the distribution of FMXene on the aluminium surface were examined by SEM, providing visual evidence to support the proposed self-assembly mechanism. Fig. 3a and b show the as-prepared MMXene, which exhibits an accordion-like structure, indicative of its layered morphology that facilitates efficient exfoliation and high interlayer accessibility. After 1 h of ultrasonic treatment, the MMXene is exfoliated into few-layer FMXene (2–5 layers), as shown in Fig. 3c and d. The SEM images reveal that the exfoliated FMXene sheets possess a high aspect ratio, with a width of approximately 50–100 μm and a thickness of around 500 nm. By comparison, MMXene retains a much thicker multilayered structure, with an average layer number estimated to be approximately10 times higher, as evidenced by the pronounced thickness difference observed in the SEM images. Fig. 3e and f display the irregularly shaped aluminium powders, with particle sizes ranging from 50 to 125 μm. A closer examination of Fig. 3g and h reveals that, in the 0.5FMXene-Al composite, the soft FMXene sheets conform closely to the surface topography of the aluminium particles, forming a continuous and intimate coating.

The regions highlighted by blue dashed circles in Fig. 3g mark typical areas where the FMXene nanosheets are observed wrapping around the aluminium particle surface, while Fig. 3h presents a magnified view of red region in Fig. 3g, clearly showing the wrinkled and layered morphology of the FMXene coating. This conformal coverage modifies the surface texture rather than altering the overall morphology of the aluminium powders, which reflects the typical nature of the self-assembly process. Such good interfacial contact indicates effective coating of FMXene and is expected to enhance the mechanical integrity and structural stability of the FMXene-Al composites.

X-ray photoelectron spectroscopy (XPS) is a powerful tool for detecting surface elements and confirming the presence of functional groups on aluminium and FMXene surfaces. The chemical valence and elemental composition of the aluminium and FMXene were analysed by XPS, and the results are shown in Fig. 4. Fig. 4a displays the XPS survey spectra of aluminium and FMXene powders. The spectra confirm the presence of key elements, including Al, O, Ti and C, as well as minor traces of fluorine (F) in FMXene. Fig. 4b and c represent the high-resolution XPS spectra of Al 2p and O 1 s of aluminium, respectively. As shown in Fig. 4b, the XPS peak at 74.48 eV is attributed to Al_2O_3, while the two additional peaks at 72.54 eV and 72.13 eV correspond to metallic aluminium (Al). Since XPS primarily detects the sample surface,

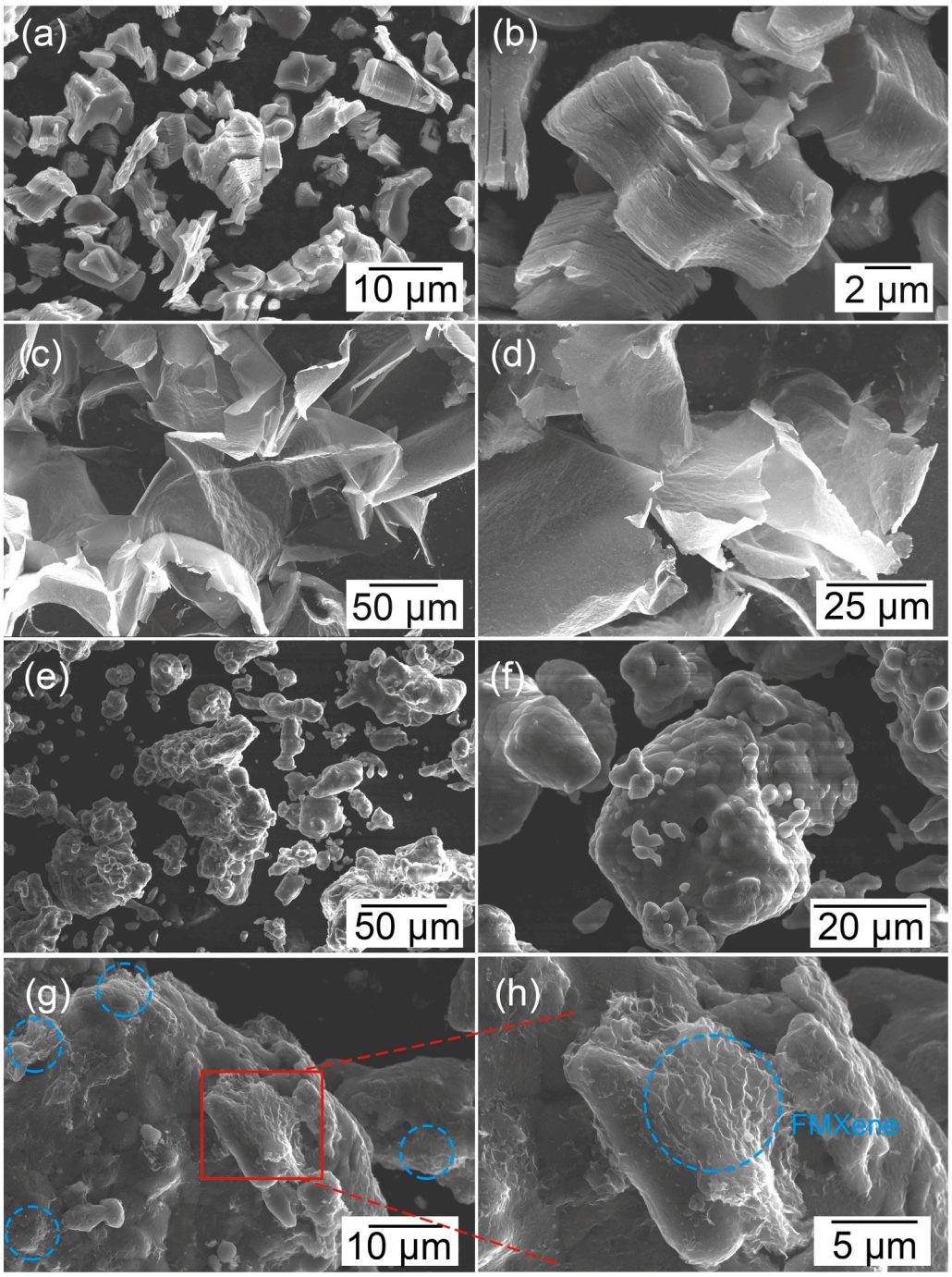

Fig. 3. (a, b) Multi-layer MXene; (c, d) After 1-hour ultrasonic treatment to adjust few-layer MXene; (e, f) Aluminium powder; (g, h) 0.5FMXene-Al composites.

the intensity of Al_2O_3 is higher compared to metallic Al, indicating the presence of an oxide layer on the surface. Fig. 4c shows the XPS spectrum of O 1 s, which is deconvoluted into three distinct peaks at approximately 531, 531.58, and 532.08 eV [36]. These peaks are assigned to Al-O, carbonate and -OH bonds, respectively, confirming the presence of hydroxyl (-OH) groups on the surface of aluminium. Fig. 4d, e and f represent the high-resolution XPS spectra of Ti 2p, C 1 s, and O 1 s regions for the FMXene sample, respectively. In Fig. 4d, the Ti 2p spectrum shows that the Ti-C bond has the highest peak intensity, indicating the predominant presence of Ti in the carbide form. The presence of a minor peak at 485.5 eV, attributed to Ti^{4+} (TiO_2), has the lowest intensity among the Ti peaks, suggesting minimal oxidation of titanium [37,38]. This indicates that the FMXene structure remains intact with limited degradation, and only a small amount of TiO_2 has formed. Fig. 4e illustrates the high-resolution C1s spectrum, which shows peaks attributed to Ti-C, Ti-C-O, C-C, C-O and C═O bonds. Notably, the Ti-C peak exhibits the highest intensity, further confirming the stability of the FMXene carbide structure [39]. The presence of C-O and C═O bonds suggest surface oxidation or functionalization, but their relatively low intensity implies that most carbon atoms are still bonded to titanium. Fig. 4f presents the O1s spectrum, deconvoluted into four peaks corresponding to four oxygen environments, including Ti-O, C═O, C-O, and a minor peak attributed to -COOH groups. The Ti-O indicates titanium oxide, while the presence of C-O, C═O and -COOH indicates the surface functional groups. These oxygen-containing groups can establish interfacial interactions with the hydroxylated aluminium

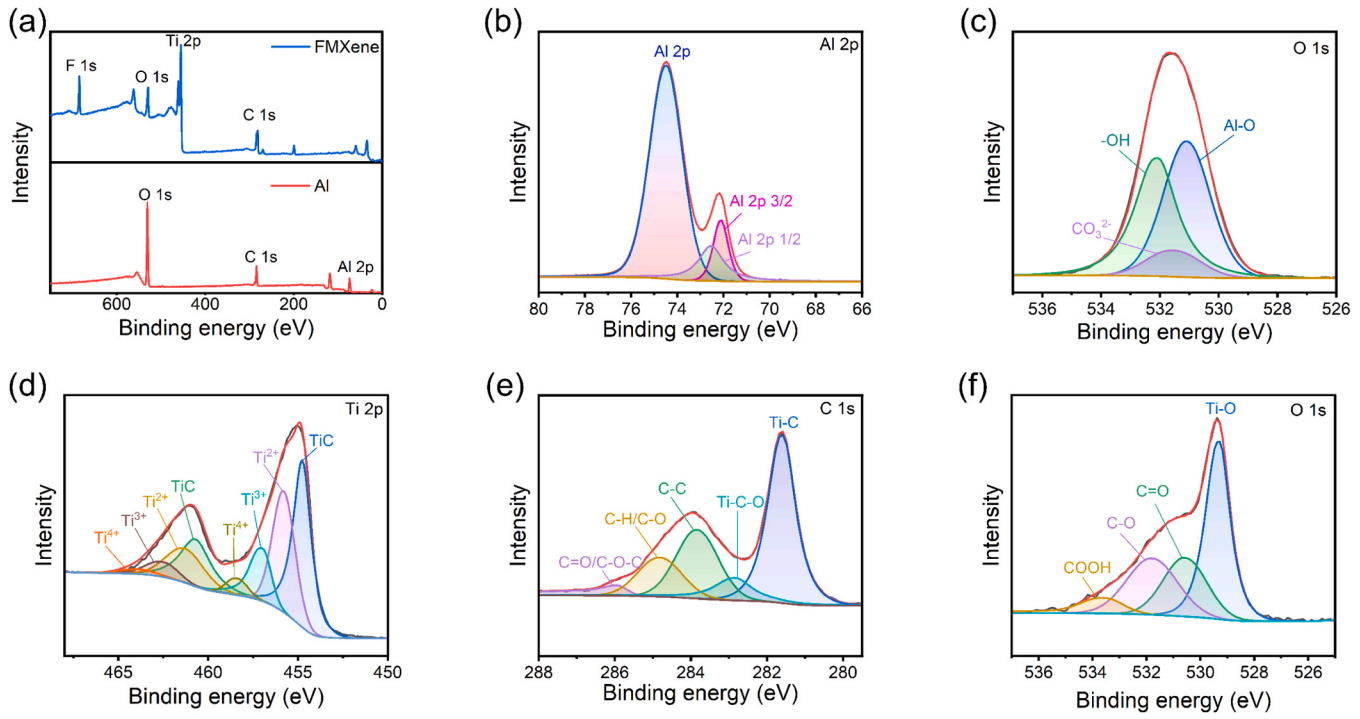

Fig. 4. (a) XPS spectra of aluminium and FMXene; (b, c) High-resolution Al 2p and O 1 s spectra of aluminium powder; (d, e, f) High-resolution Ti 2p; C 1 s, and O 1 s spectra of FMXene powder.

surface, leading to improved interfacial compatibility and bonding strength. These results provide strong support for the self-assembly strategy, confirming that the interfacial bonding is chemically driven by complementary functional groups on both materials. The confirmed uniform adhesion of FMXene on aluminium particles plays a crucial role in enhancing the mechanical performance of the composites [40,41].

3.2. Mechanical properties of HPT-processed FMXene- and MMXene-Al composites

To further evaluate the mechanical performance of the HPT-processed composites, microhardness measurements were carried out. Given the shear inhomogeneity resulting from HPT, where the shear strain applied to the sample edges surpasses that at the centre, the mechanical response across the entire sample is expected to vary from the central region to the periphery [30,42]. Fig. 5a, b, c and d show the microhardness profiles of pure Al, 5MMXene-Al, 1FMXene and 0.5FMXene composites, respectively, processed by HPT with varying numbers of turns, ranging from 0 to 20. The 5FMXene-Al composite, which exhibited severe brittleness during HPT processing, is not included here, the corresponding microhardness tests are provided in the Fig. S2. In the overall observation of the microhardness profiles, the hardness values exhibit a relatively stable distribution from the centre to the edge at 0 turn, with the average values for pure aluminium and 5MMXene-Al composites approximately 55 HV, whereas the average values for 1FMXene-Al and 0.5FMXene-Al composites are approximately 60 HV. This difference can be attributed to the structural configuration of MMXene and FMXene within the composites. Specifically, the FMXene tends to wrap around the aluminium particles, thereby providing improved surface coverage and enabling efficient load transfer even in the absence of torsion strain (0 turn). In contrast, the micro-scale MMXene is merely physically mixed with the aluminium matrix, contributing less effectively to interfacial bonding and mechanical strengthening [43,44]. As the number of HPT turns increases to 1, 5 and 20, the hardness values of all samples show a gradual rise, with a noticeable increase from the centre to the edge. The observed hardness increment is primarily due to shear strain induced by HPT, which introduces significant strain gradients and grain refinement throughout the materials [45], The underlying microstructure mechanisms responsible for this behaviour will be discussed in detail in the following EBSD section. Moreover, the disparity in hardness between the edge and centre becomes increasingly pronounced with more HPT turns, except for pure aluminium. As illustrated in Fig. 5a and supported by prior study [46], pure aluminium exhibits relatively uniform hardness distribution after HPT, with only a slight increase from centre to the edge. This minor gradient can be attributed to the non-uniform shear strain imposed during HPT, which generates higher dislocation density and finer grains at the periphery even in the absence of reinforcement particles. However, owing to the high stacking fault energy of aluminium, dislocations are highly mobile, and dynamic recovery is readily activated at room temperature, which limits the extent of strain hardening and leads to only minor hardness variation across the sample.

In contrast, the incorporation of MMXene (FMXene) as a reinforcing phase plays a pivotal role in enhancing the hardness of the aluminium matrix composites, though their effectiveness differs significantly. Notably, the hardness of the 1FMXene-Al composite (Fig. 5c) reaches a maximum of 140 HV, surpassing that of the 5MMXene-Al composite (Fig. 5b), which only achieves a maximum of 110 HV. Interestingly, even the 0.5FMXene-Al composite (Fig. 5d) attains a comparable maximum hardness of 110 HV. This behaviour can be attributed to the progressively uniform dispersion of FMXene as the number of HPT turns increases. Although HPT introduces significant shear strain, it may still be insufficient to fully exfoliate and uniformly disperse the thicker MMXene into few-layer structures, which could explain its relatively lower reinforcing efficiency. In contrast, the thinner FMXene sheets are more susceptible to tearing and fragmentation under severe shear deformation, generating numerous nanoscale fragments that act as effective dislocation barriers. These fragments promote dislocation multiplication through Frank-Read sources and enhance Orowan looping, further strengthening the matrix. Meanwhile, the intrinsic large specific surface area of FMXene promotes efficient load transfer and further restricts dislocation motion at the FMXene/Aluminium interface

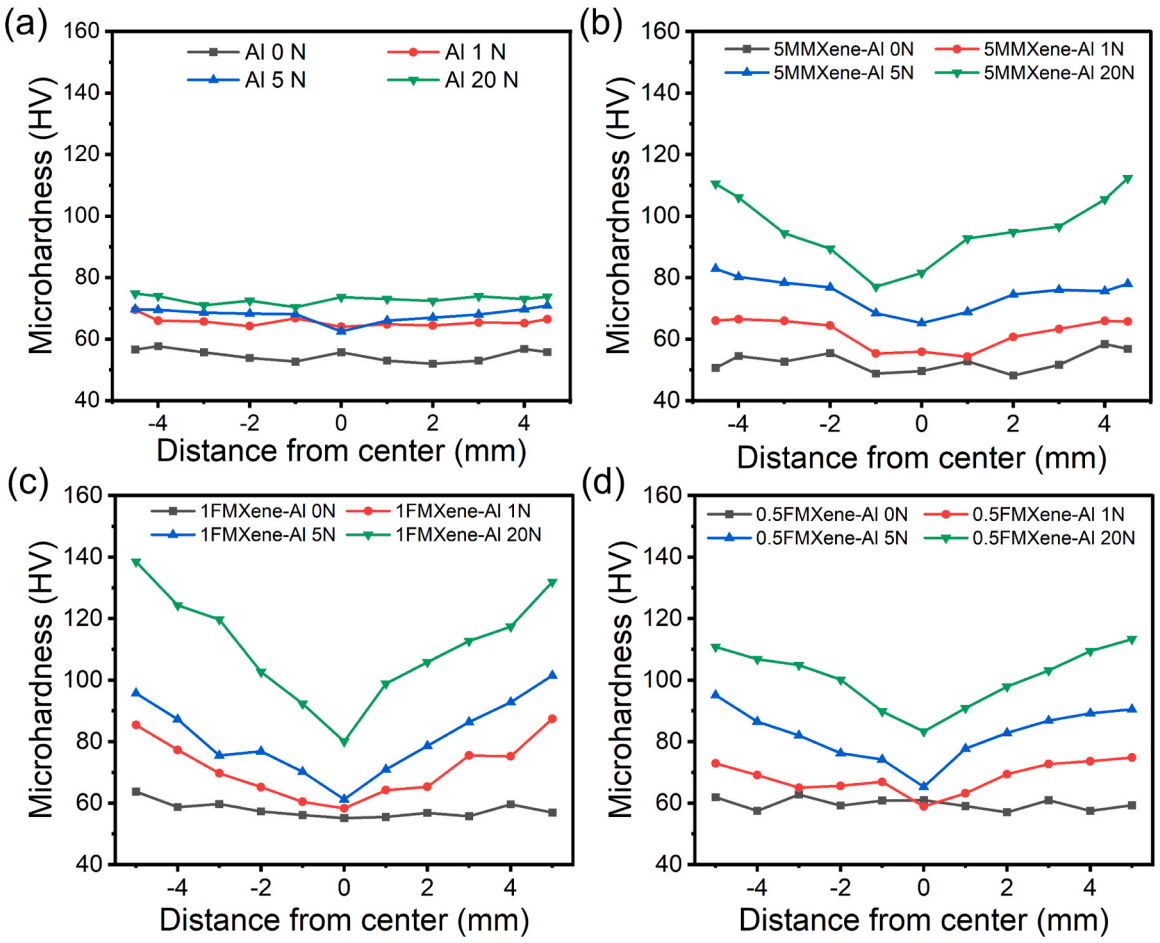

Fig. 5. Vickers microhardness profiles of (a) Pure Al; (b) 5MMXene-Al composites; (c) 1FMXene-Al composites and (d) 0.5FMXene-Al composites processed by HPT with different numbers of turns (0–20).

[10]. The combined effects of these mechanisms lead to superior overall hardening, confirming that FMXene is more efficient than MMXene as a reinforcing phase in AMCs

Fig. 6 presents the engineering strain-stress curves of pure aluminium, 5MMXene-Al, 1FMXene-Al and 0.5FMXene-Al composites, while the corresponding mechanical parameters, including yield strength, ultimate tensile strength and total elongation, are summarized in Table 1. Pure aluminium (Fig. 6a) exhibits a ductile behaviour with a total elongation of up to 1.91 % after 20 HPT turns, but its yield strength and ultimate tensile strength remain relatively low, with maximum values of 197 MPa and 244 MPa, respectively. The incorporation of MMXene and FMXene as reinforcing phases significantly enhances the yield strength and ultimate tensile strength of the aluminium matrix composites. For instance, after 20 turns, the yield strength of 5MMXene-Al (Fig. 6b) and 0.5FMXene-Al (Fig. 6d) composites reach 257 MPa and 242 MPa, while the ultimate tensile strength of these composites increases to 294 MPa and 291 MPa, respectively. However, this improvement in strength comes at the expense of ductility, both 5MMXene-Al and 0.5FMXene-Al composites exhibit reduced total elongation compared to pure aluminium, with values of 0.89 % and 0.857 %, respectively, after 20 turns. Despite the reduced elongation, both 0.5 FMXene-Al and 5MMXene-Al composites exhibits approximately 1.3 times higher strength than pure aluminium after 20 turns. It is noteworthy that the 0.5FMXene-Al composite achieves nearly equivalent strength to the 5MMXene-Al composite while requiring only one-tenth of the reinforcement content. This demonstrates that the superior reinforcement efficiency of FMXene, which is attributed to its higher specific surface area and stronger interfacial bonding with aluminium matrix.

To further evaluate the effect of FMXene content, the tensile behaviour of the 1FMXene-Al composites was also investigated, as shown in Fig. 6c. The results reveal that the 1FMXene-Al composite exhibits tensile strength of 114.8, 178.3 and 192.9 MPa after 1, 5 and 20 turns, respectively, accompanied by negligible ductility across all conditions. The relatively low tensile strength and brittle failure of the 1FMXene-Al composites are likely caused by excessive incorporation of FMXene. While moderate FMXene content is well dispersed within the aluminium matrix under the severe plastic deformation induced by HPT, which contributes to an increase in dislocation density and improves the load-bearing capacity of the composite. However, when the FMXene content is excessive, the high aspect ratio of FMXene tends to agglomerate within the matrix. These aggregates act as stress concentrators, facilitating the premature initiation and propagation of cracks under tensile loading, thereby compromising the overall mechanical performance [47–49]. Considering the above-mentioned hardness and tensile test results, the 0.5FMXene-Al composite exhibits the most favourable combination of mechanical performance and structural integrity. Furthermore, its low reinforcement content provides a clear economic advantage compared to higher-load formulations. Therefore, subsequent analyses in this study focus primarily on the 0.5FMXene-Al composites as the optimal system.

3.3. The distribution of MMXene and FMXene in the Al matrix after HPT processing

To further elucidate the origin of the enhanced mechanical

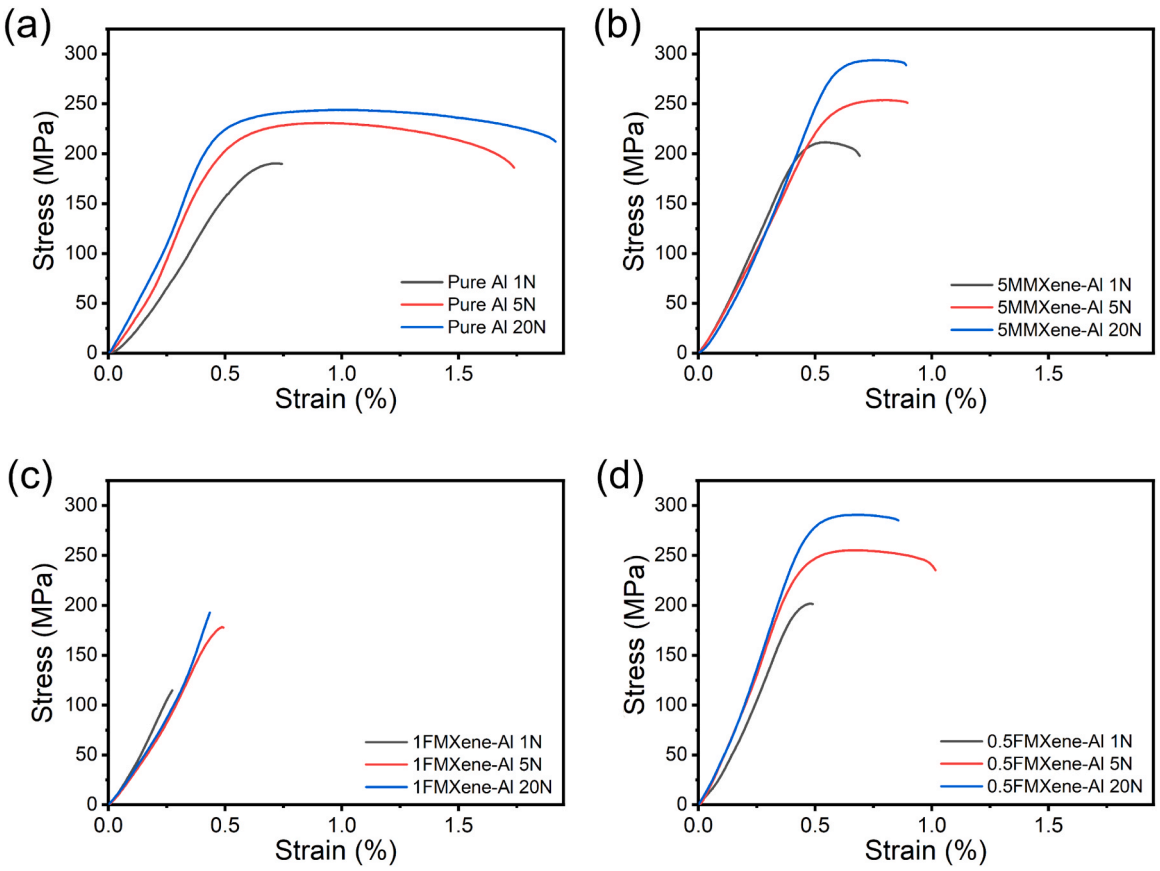

Fig. 6. Engineering stress-strain curves of (a) Pure Al; (b) 5MMXene-Al composites; (c) 1FMXene-Al composites and (d) 0.5FMXene-Al composites processed by HPT with 1, 5 and 20 turns.

Table 1
The yield strength, ultimate tensile strength, total elongation extracted from Engineering stress-strain curves.

Sample	Yield Strength (MPa)	Ultimate tensile strength (MPa)	Total Elongation (%)
Pure Al 1 N	159	190.2	0.74
Pure Al 5 N	177	230.84	1.74
Pure Al 20 N	197	243.89	1.91
5MMXene-Al 1 N	175.52	211.4	0.69
5MMXene-Al 5 N	207.17	253.72	0.9
5MMXene-Al 20 N	257.11	293.7	0.89
1FMXene-Al 1 N	N/A	114.8	0.27
1FMXene-Al 5 N	N/A	178.3	0.49
1FMXene-Al 20 N	N/A	192.86	0.43
0.5MXene-Al 1 N	181.35	201.7	0.49
0.5MXene-Al 5 N	213.27	255.22	1.01
0.5MXene-Al 20 N	242.45	290.71	0.86

properties, detailed microstructural analyses were carried out on the HPT-processed composite discs using SEM, TEM, XRD and EBSD. Fig. 7a, b and c show the SEM images of 5MMXene-Al composites processed by HPT for 1, 5 and 20 turns in the edge region. It can be observed that the shape and morphology of MMXene remain largely unchanged as the HPT turns increase from 1 N to 20 N. This suggests that the applied shear stress during the HPT process is insufficient to induce exfoliation or delamination of MMXene. This observation may explain the relatively lower reinforcing efficiency of MMXene compared to FMXene in mechanical properties. Moreover, MMXene, as a micro-scale material, is inherently well-dispersed and resistant to aggregation, reducing the effectiveness of HPT in further improving dispersion [43,50]. Consequently, the lack of exfoliation and the natural dispersion of MMXene limit its reinforcing effect in the aluminum matrix, resulting in modest improvements in mechanical properties. Fig. 7d, e and f indicate the SEM images of 0.5FMXene-Al composites processed by HPT for 1, 5 and 20 turns in the edge region. The noticeable agglomeration of FMXene can be observed at 1 N. As the number of HPT turns increases to 5 and 20, the agglomerated FMXene is progressively fragmented into much smaller particles and becomes more uniformly dispersed within the matrix, compared to the sample processed at 1 N. This indicates that the shear deformation induced by HPT effectively promotes FMXene flow and facilitates the fragmentation of FMXene agglomerates within the matrix.

To further support this observation, a quantitative SEM-based analysis was performed on the images in Fig. 7d-f, and the corresponding fragment size distributions are provided in Fig. S3. The average equivalent diameter of fragments decreases markedly from approximately 10 μm at 1 turn to ~ 1.9 μm after 5 turns, indicating rapid fragmentation of initial agglomerates. With further deformation to 20 turns, the fragments are further refined to an average diameter of ~ 1.4 μm. This quantitative trend confirms the progressive fragmentation of FMXene under HPT and is consistent with the observed improvement in dispersion and reinforcement efficiency. However, it is important to note that increasing the content of FMXene in the aluminium matrix to some extent could lead to significant agglomeration due to the strong van der Waals forces and the inherent tendency of FMXene to cluster at higher

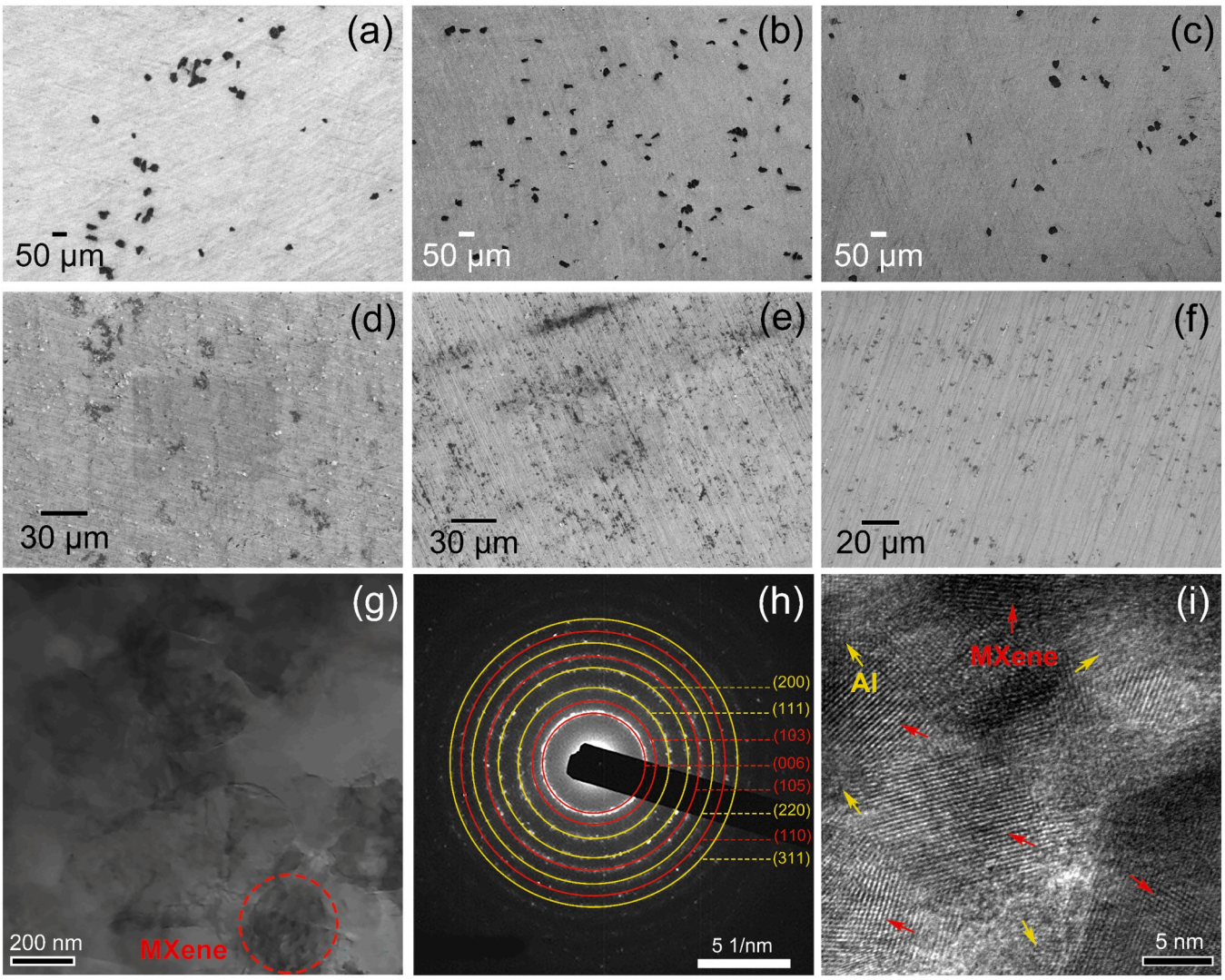

Fig. 7. (a-c) SEM images of the 5MMXene-Al composites after 1, 5 and 20 turns in the edge region; (d-f) SEM images of the 0.5FMXene-Al composites after 1, 5 and 20 turns in the edge region; (g-i) TEM, SAED, and HRTEM images of the 0.5 FMXene-Al composite after 20 turns.

concentrations. As shown in Fig. S4, the SEM images of 5FMXene-Al composites processed by HPT for 0, 1 and 5 turns reveal noticeable FMXene agglomeration, indicating that the imposed shear strain is insufficient to achieve uniform dispersion at high FMXene content. This observation is consistent with the brittle fracture behaviour of the 5FMXene-Al composites discussed earlier. The high content of FMXene not only hinders the uniform dispersion of FMXene but also reduces the overall reinforcing efficiency by introducing stress concentration points within the matrix. Thus, maintaining a balance between the reinforcement content and its dispersion is crucial to maximizing the overall performance of the materials.

Fig. 7g-i depicts the TEM characterization of 0.5FMXene-Al composite processed by HPT for 20 turns. The darker regions (highlighted by the red dash circle) in Fig. 7g are attributed to the dispersed FMXene sheets, whereas the brighter regions correspond to the aluminium matrix. Based on these observations, TEM analysis further reveals that the FMXene nanosheets are homogeneously distributed within the aluminium matrix, indicating an effective dispersion achieved through HPT processing. To confirm the identity of the dark regions, selected area electron diffraction (SAED) was conducted on these areas, as shown in Fig. 7h. The diffraction rings can be indexed to both FCC-Al and $Ti_3C_2T_x$ MXene phase. The rings marked in red correspond to the (006), (103), (105) and (110) planes of MXene [51–53], while those highlighted in yellow correspond to the (111), (200), (220) and (311) planes of aluminium. This confirms that the darker regions in Fig. 7g originate from FMXene. High-resolution TEM (HRTEM) analysis was conducted further performed to elucidate the interfacial structure between FMXene and aluminium, as shown in Fig. 7i. The HRTEM image reveals well-defined lattice fringes with an interplanar spacing of approximately 0.34 nm, corresponding to the (006) planes of MXene [54], as indicated by the red arrows. Additionally, lattice fringes with a spacing of ~ 0.23 nm, corresponding to the (111) planes of FCC-Al [55], are also observed (marked by yellow arrows). The aluminium lattice fringes appear slightly distorted and less distinct, which can be attributed to the high shear strain and lattice distortion introduced during HPT processing. The coexistence of both lattice fringes within the same region provides direct evidence of the intimate interfacial contact between FMXene and the aluminium matrix, further confirming the uniform dispersion and strong interfacial bonding achieved in the composite.

3.4. Microstructure evolution of 0.5 FMXene-Al composites during HPT processing

To provide insights into the strengthening mechanism, X-ray diffraction (XRD) was conducted to identify the microstructural phases

responsible for the observed enhancement.

Fig. 8 shows XRD patterns of the HPT-processed 0.5FMXene-Aluminum samples at 1, 5 and 20 N, all diffraction peaks agree well with the aluminium standard diffraction pattern, corresponding to (111), (200), (220), (311) and (222) planes at 2θ values of 38.61°, 44.83°, 65.19°, 78.3° and 82.35°, respectively. No Al_4C_3 or other reaction products were detected, confirming that no interfacial reaction occurred during the HPT process. The absence of Ti_3C_2 peaks is attributed to the fact that XRD can only detect high concentrations of FMXene (>10 wt%) in FMXene-Al composites, as the limited number of stacked $Ti_3C_2T_x$ layers leads to very weak diffraction signals [17]. All peaks reveal a conspicuous decrease in intensity and a broadening of peaks with the increase of number of rotations, indicating the microstructure refinement in aluminium matrix. Additionally, according to the Scherrer formula [56,57]:

$$D = \frac{K\lambda}{\beta\cos\theta} \quad (1)$$

Where D is the crystallite size, K is a constant number, taken as 0.89, λ is the X-ray wavelength, taken as 0.154, β is the full width at half maximum (FWHM) of the diffraction peak and θ is the diffraction angle of X-rays. By combining the Scherrer equation with X-ray diffraction (XRD) data, the crystallite size, dislocation density and microstrain can be calculated, which is summarized in Table 2. With increasing numbers of HPT turns, a gradual refinement of the crystallite size is observed, accompanied by an increase in dislocation density and microstrain. Notably, no systematic shift in the Al diffraction peak positions is detected among the FMXene-Al composites processed for different number of turns, indicating that FMXene fragmentation does not lead to detectable elemental dissolution into the Al matrix. Therefore, the observed peak broadening is mainly attributed to lattice distortion associated with dislocation accumulation and microstrain. This trend is consistent with the enhanced microhardness and strength of the FMXene-Al composites, which arise from the combined effects of grain refinement, increased dislocation density and lattice strain induced by HPT and FMXene.

Fig. 9 and Table 3 provide a clear illustration of the microstructural evolution of the 0.5FMXene-Al composite processed by HPT at different numbers of rotations (1 N, 5 N and 20 N), including EBSD maps taken from both the centre and edge regions, with the sampling positions indicated schematically in Fig. S5. The EBSD map are presented as pseudo-3D inverse pole figure (IPF) orientation maps, in which the top, left, and front faces of each cube correspond to the X, Y, and Z directions of the sample, respectively. The colour legend indicates the crystallographic orientation according to the standard IPF triangle. To more

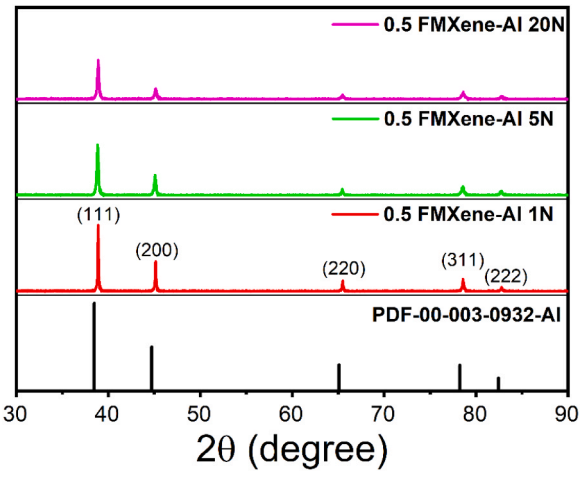

Fig. 8. X-ray diffraction patterns of 0.5FMXene-Al composites processed by HPT with 1, 5 and 20 N.

Table 2
Crystallite size, dislocation density and microstrain after HPT process.

Sample	Crystallite size (nm)	Dislocation density (m^{-2})	Microstrain (10^{-3})
1 N	54.98	3.31×10^{14}	1.29
5 N	31.22	1.03×10^{15}	2.30
20 N	27.21	1.35×10^{15}	2.62

precisely capture the intermediate stage of the microstructural evolution, an additional sample processed for 10 turns was also examined, and the corresponding EBSD are presented in Fig. S6. The average gain sizes of HPT-processed samples were summarized in Table 3, which shows that both centre and edge regions exhibit pronounced grain refinement with increasing torsional strain. In the centre region, the average size decreases from 1.1 μm at 1 N to 0.4 μm at 20 N, while the fraction of high-angle grain boundaries (HAGBs) increases from 62.4 % to 88.5 %. In contrast, the edge region undergoes faster refinement, reaching a saturated grain size of 0.4 μm and HAGB fraction of 89.9 % at 5 N. This difference arises from the gradient in shear strain across the disc and is consistent with the hardness distribution (Fig. 5d), where the edge exhibits higher hardness than the centre.

Based on the EBSD observations and grain-size evolution, the deformation process can be divided into four distinct stages. The microstructural evolution of the 0.5FMXene-Al composite during HPT is governed by the interplay between dislocation activity, recovery, and FMXene-induced interface interactions, corresponding respectively to: (i) initial plastic deformation (1 N); (ii) dynamic recrystallization; (iii) recovery-dominant stage (10 N), (iv) steady state (20 N).

At 1 turn, the disc mainly experiences initial plastic deformation, during which dislocation multiplication begins and elongated substructures form. As the number of torsional cycles increase from 1 N to 5 N, severe plastic deformation introduces an extremely high density of dislocations, leading to the subdivision of original grains into dislocation cells and sub grains. The gradual increase in misorientation among these sub grains promotes their transformation into high-angle grain boundaries (HAGBs), which explains the significant increase in HAGB fraction from 62 % at 1 turn to nearly 89 % at 5 turns [58]. This stage corresponds to the activation of continuous dynamic recrystallization (CDRX), where dislocation accumulation dominates over recovery. With further torsional straining (5–10 turns), the accumulation of plastic work generates considerable internal frictional heating, facilitating dislocation climb and annihilation. As a result, dynamic recovery becomes increasingly active and counteracts grain refinement, leading to a slight decrease in HAGB fraction, particularly at the edge where strain and temperature are highest. This behaviour is consistent with the dislocation-based steady-state model, in which the minimum attainable grain size (d_{min}) is determined by the balance between dislocation multiplication and thermally activated recovery [31,59]. According to this framework, the refinement rate decreases exponentially with increasing strain once this balance is approached. The present results reveal that the edge region reaches such a quasi-steady-state condition around 5 turns, while the centre continues to refine until 20 turns due to its lower effective strain. The incorporation of FMXene play a critical role in modifying this balance. The two-dimensional FMXene reinforcements act as strong barriers to dislocation motion and sub grain boundary migration, enhancing dislocation storage capability and delaying recovery. In addition, the FMXene/Aluminium interfaces provide preferential nucleation sites for sub grains and facilitate load transfer across the matrix-reinforcement interface, which accelerates dynamic recrystallization in the early stages but stabilizes the refined grains at later stages. Consequently, the composite achieves a finer steady-state grain size (~ 0.4 μm) compared to monolithic aluminium processed under similar conditions. Furthermore, the strain gradient across the disc induces spatial variations in texture evolution. The edge region, subjected to intense shear deformation, develops a sharper

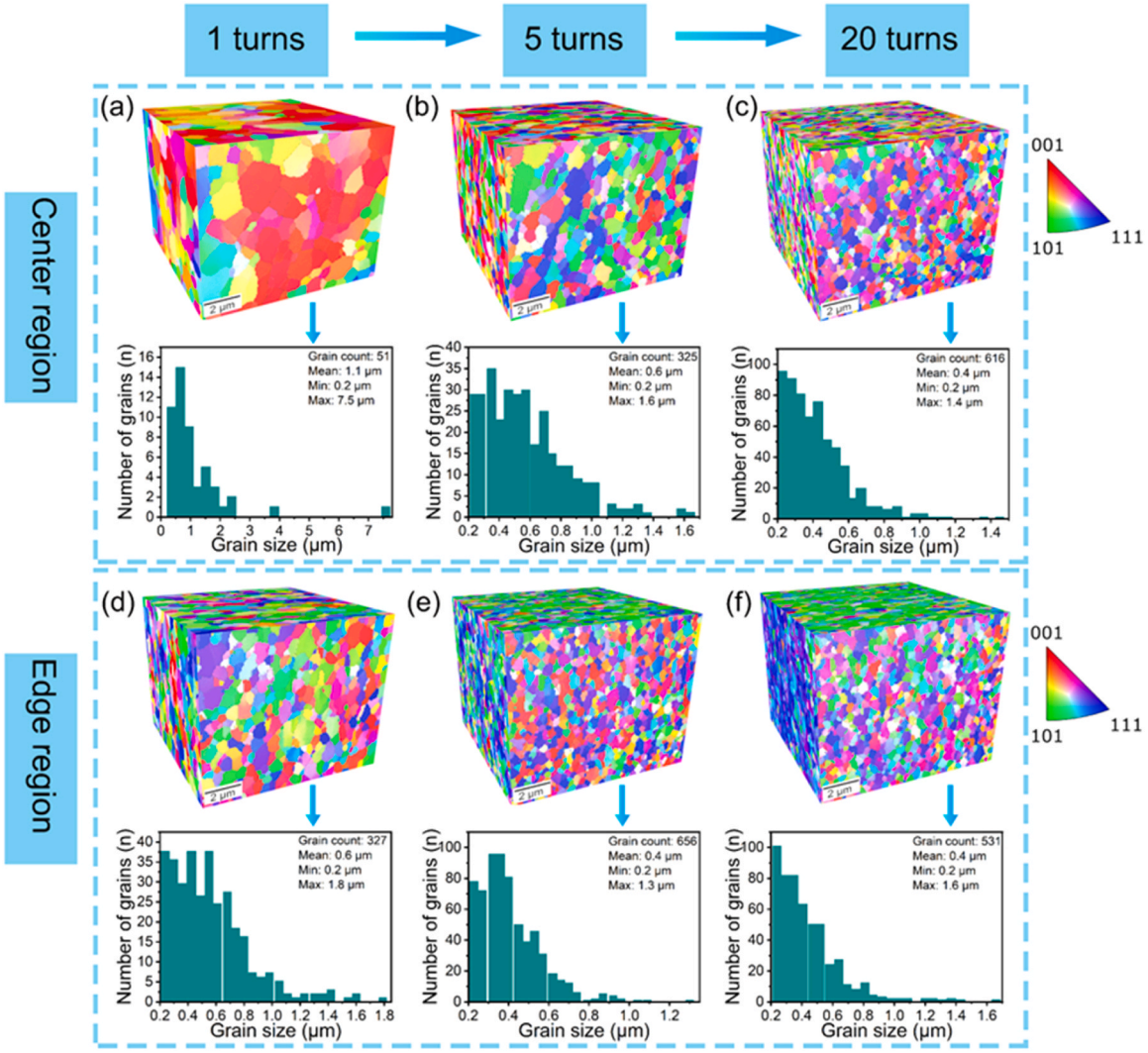

Fig. 9. Pseudo three-dimensional inverse pole figure orientation maps and corresponding grain size distribution of the 0.5FMXene-Al composite processed by HPT with different numbers of rotations: (a-c) centre region and (d-f) edge region after 1, 5 and 20 turns.

Table 3
The average grain size and HAGB fraction at the centre and edge regions after HPT process, obtained from EBSD analysis (Fig. 9).

Turns	Position	Average grain size (μm)	HAGB (%)
1 N	centre	1.1	62.4
1 N	edge	0.6	87.9
5 N	centre	0.6	88.5
5 N	edge	0.4	89.9
10 N	centre	0.5	88.1
10 N	edge	0.4	88
20 N	centre	0.4	88.4
20 N	edge	0.4	84.2

simple-shear texture as grains rotate to align $< 110 >$ or $< 111 >$ directions along the shear axis, while the centre region remains largely random in orientation. This evident texture gradient correlates well with the hardness distribution: although both the centre and edge region of the 0.5FMXene-Al composite processed for 20 turns exhibit comparable average grain size, the edge still maintains a higher hardness. This can be attributed to the combined effects of texture-induced directional strengthening and the pining effect of FMXene, which collectively contribute to a moderate degree of mechanical anisotropy in the HPT-processed composite. Overall, the microstructural evolution from dislocation accumulation to dynamic recovery and eventual stabilization reflects a dynamic balance between deformation and recovery. The presence of FMXene reinforcements shifts this balance by retarding recovery and stabilizing ultrafine grains, which ultimately contributes to the enhanced hardness and tensile strength of the composite compared with pure aluminium.

3.5. Strengthening mechanism analysis

The remarkable enhancement in strength and hardness of the 0.5FMXene-Al composites can be attributed to the synergistic action of multiple strengthening mechanisms activated during HPT. The severe plastic deformation introduced by HPT induces ultrafine grain formation, contributing to grain boundary strengthening in accordance with the Hall-Petch effect. Using the Hall-Petch relationship [60,61]:

$$\sigma_y = \sigma_0 + K_y d^{-1/2}$$

Where σ_0 is lattice friction stress, k_y is the Hall-Petch coefficient for aluminium, and d is the grain size. By adopting typical literature values for aluminium ($K_y \approx$ 0.07–0.09 MPa•m$^{1/2}$) and the experimentally measured grain size ($\sim$ 0.4 μm), the Hall-Petch term $K_y d^{-1/2}$ yields a strengthening contribution on the order of 100–150 MPa relative to coarse-grained aluminium. It should be noted that the experimentally

measured strength also includes contributions from lattice friction and HPT-induced dislocation hardening arising from the extremely high dislocation density introduced during HPT. Therefore, this estimate is consistent in magnitude with the high yield strength level achieved after HPT processing.

In addition to grain refinement, HPT promotes the homogeneous dispersion and intimate interfacial bonding of FMXene nanosheets within the aluminium matrix. These uniformly distributed FMXene nanosheets act as effective barriers to dislocation motion and facilitate load transfer across the FMXene/Al interface, thereby providing an additional strengthening increment on the order of several tens of MPa beyond the baseline strengthening induced by HPT. Moreover, FMXene nanosheets located near grain boundaries can further stabilize the refined microstructure by generating a Zener pinning effect, which suppresses grain boundary migration during deformation and recovery. This pinning effect does not dominate the strength level but contributes to maintaining the ultrafine-grained structure under high strain conditions.

The integration of these effects, including grain refinement, dislocation hardening, load transfer, and interfacial pining, leads to the formation of a multi-scale strengthening network. The FMXene/Aluminium interfaces serve as both mechanical and chemical reinforcements, optimizing strain transfer efficiency and delaying recovery. Consequently, the composite exhibits a unique balance of strength and ductility compared to conventional carbon-based reinforcements. This synergistic mechanism highlights the importance of interface engineering in the design of advanced aluminium matrix composites processed via HPT.

4. Conclusion

In this study, FMXene was successfully incorporated into an aluminium matrix via a novel electrostatic self-assembly approach, followed by consolidation through HPT at room temperature. The presence of surface functional groups on both FMXene and aluminium particles enabled strong interfacial interactions, while the intense shear strain from HPT facilitated the uniform dispersion of FMXene flakes and the formation of ultrafine-grain microstructures (~ 400 nm). Mechanical tests demonstrated that the incorporation of FMXene significantly enhanced the hardness and tensile strength of the composites, with the 0.5FMXene-Al sample showing the most balanced performance, achieving a hardness of 110 HV and an ultimate tensile strength of 291 MPa, while maintaining reasonable ductility. These improvements are attributed to the synergistic effects of enhanced interfacial bonding, efficient load transfer, grain refinement and dispersed FMXene. Overall, this work presents a promising, cost-effective pathway for designing high-performance aluminium matrix composites using 2D FMXene reinforcements, with potential applications in lightweight structural and aerospace components.

CRediT authorship contribution statement

Walaa Abd-Elaziem: Writing – review & editing, Resources, Formal analysis. **Tarek Allam:** Writing – review & editing, Resources, Formal analysis. **Abdelrahman Elsayed:** Writing – review & editing, Investigation, Formal analysis, Data curation. **Jing Ye:** Writing – review & editing, Writing – original draft, Visualization, Validation, Software, Methodology, Investigation, Formal analysis, Data curation, Conceptualization. **Yi Huang:** Writing – review & editing, Supervision, Resources, Project administration, Methodology, Investigation, Funding acquisition, Formal analysis, Conceptualization. **Abdelkader Amr M:** Writing – review & editing, Supervision, Resources, Project administration, Funding acquisition, Formal analysis, Conceptualization. **Ali Reza Kamali:** Writing – review & editing, Resources, Funding acquisition, Formal analysis.

Declaration of Competing Interest

The authors declare that they have no known competing financial interests or personal relationships that could have appeared to influence the work reported in this paper.

Acknowledgements

One of the authors (J. Ye) would like to acknowledge the financial support of Bournemouth University for the PhD studentship award, which supports this work.

Appendix A. Supporting information

Supplementary data associated with this article can be found in the online version at doi:10.1016/j.jallcom.2026.186026.

References

[1] G. Manohar, K.M. Pandey, S.R. Maity, Effect of variations in microwave processing temperatures on microstructural and mechanical properties of AA7075/SiC/graphite hybrid composite fabricated by powder metallurgy techniques, Silicon 14 (2022) 7831–7847.
[2] M.R. Mattli, P.R. Matli, A. Shakoor, A.M. Amer Mohamed, Structural and mechanical properties of amorphous Si_3N_4 nanoparticles reinforced Al matrix composites prepared by microwave sintering, Ceramics 2 (2019) 126–134.
[3] A. Azarniya, A. Azarniya, S. Sovizi, H.R.M. Hosseini, T. Varol, A. Kawasaki, S. Ramakrishna, Physicomechanical properties of spark plasma sintered carbon nanotube-reinforced metal matrix nanocomposites, Prog. Mater. Sci. 90 (2017) 276–324.
[4] J. Dong, N. Gao, Y. Chen, L. Cao, H. Song, H. Fröck, B. Milkereit, M.J. Starink, Achieving ultra-high strength of Al-Cu-Li alloys by the combination of high pressure torsion and age-hardening, Materials Science Engineering A 832 (2022) 142504 (Article).
[5] W. Zhou, Z. Zhou, Y. Fan, N. Nomura, Significant strengthening effect in few-layered MXene-reinforced Al matrix composites, Mater. Res. Lett. 9 (2020) 148–154.
[6] M. Li, S. Wang, Q. Wang, F. Ren, Y. Wang, Preparation, microstructure and tensile properties of two dimensional MXene reinforced copper matrix composites, Mater. Sci. Eng. A 803 (2021) 140699 (Article).
[7] L.-J. Zhang, F. Qiu, J.-G. Wang, Q.-C. Jiang, High strength and good ductility at elevated temperature of nano-SiC_p/Al2014 composites fabricated by semi-solid stir casting combined with hot extrusion, Mater. Sci. Eng. A 626 (2015) 338–341.
[8] Z. Baig, O. Mamat, M. Mustapha, Recent progress on the dispersion and the strengthening effect of carbon nanotubes and graphene-reinforced metal nanocomposites: a review, Crit. Rev. Solid State Mater. Sci. 43 (2016) 1–46.
[9] Z. Zhao, P. Bai, W. Du, B. Liu, D. Pan, R. Das, C. Liu, Z. Guo, An overview of graphene and its derivatives reinforced metal matrix composites: preparation, properties and applications, Carbon 170 (2020) 302–326.
[10] F. Zhang, J. Wang, T. Liu, C. Shang, Enhanced mechanical properties of few-layer graphene reinforced titanium alloy matrix nanocomposites with a network architecture, Mater. Des. 186 (2020) 108330 (Article).
[11] J. Liu, U. Khan, J. Coleman, B. Fernandez, P. Rodriguez, S. Naher, D. Brabazon, Graphene oxide and graphene nanosheet reinforced aluminium matrix composites: powder synthesis and prepared composite characteristics, Mater. Des. 94 (2016) 87–94.
[12] P. Lava Kumar, A. Lombardi, G. Byczynski, S.V.S. Narayana Murty, B.S. Murty, L. Bichler, Recent advances in aluminium matrix composites reinforced with graphene-based nanomaterial: a critical review, Prog. Mater. Sci. 128 (2022) 100948 (Article).
[13] C. Rong, T. Su, Z. Li, T. Chu, M. Zhu, Y. Yan, B. Zhang, F.Z. Xuan, Elastic properties and tensile strength of 2D $Ti_3C_2T_x$ MXene monolayers, Nat. Commun. 15 (2024) 1566 (Article).
[14] A. Lipatov, H. Lu, M. Alhabeb, B. Anasori, A. Gruverman, Y. Gogotsi, A. Sinitskii, Elastic properties of 2D $Ti_3C_2T_x$ MXene monolayers and bilayers, Sci. Adv. 4 (2018) eaat0491. (Article).
[15] K.L. Firestein, J.E. von Treifeldt, D.G. Kvashnin, J.F.S. Fernando, C. Zhang, A. G. Kvashnin, E.V. Podryabinkin, A.V. Shapeev, D.P. Siriwardena, P.B. Sorokin, D. Golberg, Young's modulus and tensile strength of Ti_3C_2 MXene nanosheets As revealed by in situ TEM probing, AFM nanomechanical mapping, and theoretical calculations, Nano Lett. 20 (2020) 5900–5908.
[16] G. Lv, W. Qian, H. Zhang, Y. Su, P. Qian, Role of –O functional groups at the $Ti_3C_2O_2$(MXene)/Al interface in enhancing the mechanical properties of aluminum matrix composites: a first-principles study, Appl. Surf. Sci. 642 (2024) 158608 (Article).
[17] B.C. Wyatt, B. Anasori, Self-assembly and in-situ characterization of $Ti_3C_2T_x$ in Al: a step toward additive manufacturing of MXene-metal composites, Appl. Mater. Today 27 (2022) 101451 (Article).

[18] M. Naguib, M. Kurtoglu, V. Presser, J. Lu, J. Niu, M. Heon, L. Hultman, Y. Gogotsi, M.W. Barsoum, Two-dimensional nanocrystals produced by exfoliation of Ti_3AlC_2, Adv. Mater. 23 (2011) 4248–4253.
[19] J. Zou, J. Wu, Y. Wang, F. Deng, J. Jiang, Y. Zhang, S. Liu, N. Li, H. Zhang, J. Yu, T. Zhai, H.N. Alshareef, Additive-mediated intercalation and surface modification of MXenes, Chem. Soc. Rev. 51 (2022) 2972–2990.
[20] J. Hu, S. Li, J. Zhang, Q. Chang, W. Yu, Y. Zhou, Mechanical properties and frictional resistance of Al composites reinforced with $Ti_3C_2T_x$ MXene, Chin. Chem. Lett. 31 (2020) 996–999.
[21] M. Li, S. Wang, Q. Wang, F. Ren, Y. Wang, Microstructure and tensile properties of Ni nano particles modified MXene reinforced copper matrix composites, Materials Science Engineering A 808 (2021) 140932 (Article).
[22] W. Zhou, Z. Zhou, S. Guo, Y. Fan, N. Nomura, Structural evolution mechanism during 3D printing of MXene-reinforced metal matrix composites, Compos. Commun. 29 (2022) 101034 (Article).
[23] Z. Hu, F. Chen, J. Xu, Q. Nian, D. Lin, C. Chen, X. Zhu, Y. Chen, M. Zhang, 3D printing graphene-aluminum nanocomposites, J. Alloy. Compd. 746 (2018) 269–276.
[24] M. Rashad, F. Pan, Y. Liu, X. Chen, H. Lin, R. Pan, M. Asif, J. She, High temperature formability of graphene nanoplatelets-AZ31 composites fabricated by stir-casting method, J. Magnes. Alloy. 4 (2016) 270–277.
[25] F. Khodabakhshi, S.M. Arab, P. Švec, A.P. Gerlich, Fabrication of a new Al-Mg/graphene nanocomposite by multi-pass friction-stir processing: dispersion, microstructure, stability, and strengthening, Mater. Charact. 132 (2017) 92–107.
[26] W. Zhou, Z. Zhou, K. Kubota, H. Ono, N. Nomura, A. Kawasaki, Design of high-performance Al_4C_3/Al matrix composites for electric conductor, Materials Science Engineering A 798 (2020) 140331 (Article).
[27] W. Zhou, T. Yamaguchi, K. Kikuchi, N. Nomura, A. Kawasaki, Effectively enhanced load transfer by interfacial reactions in multi-walled carbon nanotube reinforced Al matrix composites, Acta Mater. 125 (2017) 369–376.
[28] J. Wan, B. Chen, D. Feng, L. Cao, J. Shen, B. Guo, J.S. Li, Strengthening efficiency competition between carbon nanotubes (CNTs) and in-situ Al_4C_3 nanorods in CNTs/Al composites influenced by alumina characteristics, Composites Part A Applied Science Manufacturing 152 (2022) 106704 (Article).
[29] R.Z. Valiev, T.G. Langdon, The art and science of tailoring materials by nanostructuring for advanced properties using SPD techniques, Adv. Eng. Mater. 12 (2010) 677–691.
[30] Y. Huang, P. Bazarnik, D. Wan, D. Luo, P.H.R. Pereira, M. Lewandowska, J. Yao, B. E. Hayden, T.G. Langdon, The fabrication of graphene-reinforced Al-based nanocomposites using high-pressure torsion, Acta Mater. 164 (2019) 499–511.
[31] H. Kim, H. Ha, J. Lee, S. Son, H.S. Kim, H. Sung, J.B. Seol, J.G. Kim, Outstanding mechanical properties of ultrafine-grained Al7075 alloys by high-pressure torsion, Materials Science Engineering A 810 (2021) 141020 (Article).
[32] Y. Xie, X. Meng, D. Mao, Z. Qin, L. Wan, Y. Huang, Homogeneously dispersed graphene nanoplatelets as long-term corrosion inhibitors for aluminum matrix composites, ACS Appl. Mater. Interfaces 13 (2021) 32161–32174.
[33] J. Evertsson, F. Bertram, F. Zhang, L. Rullik, L.R. Merte, M. Shipilin, M. Soldemo, S. Ahmadi, N. Vinogradov, F. Carlà, J. Weissenrieder, M. Göthelid, J. Pan, A. Mikkelsen, J.O. Nilsson, E. Lundgren, The thickness of native oxides on aluminum alloys and single crystals, Appl. Surf. Sci. 349 (2015) 826–832.
[34] Q. Liu, M. He, X. Xu, L. Zhang, J. Yu, Self-assembly of graphene oxide on the surface of aluminum foil, N. J. Chem. 37 (2013) 181–187.
[35] Z. Li, G. Fan, Z. Tan, Q. Guo, D. Xiong, Y. Su, Z. Li, D. Zhang, Uniform dispersion of graphene oxide in aluminum powder by direct electrostatic adsorption for fabrication of graphene/aluminum composites, Nanotechnology 25 (2014) 325601 (Article).
[36] T. Tago, N. Kataoka, H. Tanaka, K. Kinoshita, S. Kishida, XPS study from a clean surface of Al_2O_3 single crystals, Procedia Eng. 216 (2017) 175–181.
[37] Y. Cao, Q. Deng, Z. Liu, D. Shen, T. Wang, Q. Huang, S. Du, N. Jiang, C.-T. Lin, J. Yu, Enhanced thermal properties of poly(vinylidene fluoride) composites with ultrathin nanosheets of MXene, RSC Adv. 7 (2017) 20494–20501.
[38] M. Mičušík, M. Šlouf, A. Stepura, Y. Soyka, E. Ovodok, M. Procházka, M. Omastová, Aging of 2D MXene nanoparticles in air: an XPS and TEM study, Appl. Surf. Sci. 610 (2023) 155351 (Article).
[39] N. Liu, Q. Li, H. Wan, L. Chang, H. Wang, J. Fang, T. Ding, Q. Wen, L. Zhou, X. Xiao, High-temperature stability in air of $Ti_3C_2T_x$ MXene-based composite with extracted bentonite, Nat. Commun. 13 (2022) 5551 (Article).
[40] Y. Kim, J. Lee, M.S. Yeom, J.W. Shin, H. Kim, Y. Cui, J.W. Kysar, J. Hone, Y. Jung, S. Jeon, S.M. Han, Strengthening effect of single-atomic-layer graphene in metal-graphene nanolayered composites, Nat. Commun. 4 (2013) 2114 (Article).
[41] S. Zhang, P. Huang, F. Wang, Graphene-boundary strengthening mechanism in Cu/graphene nanocomposites: a molecular dynamics simulation, Mater. Des. 190 (2020) 108555 (Article).
[42] M. Kawasaki, Different models of hardness evolution in ultrafine-grained materials processed by high-pressure torsion, J. Mater. Sci. 49 (2014) 18–34.
[43] R. Casati, M. Vedani, Metal matrix composites reinforced by nano-particles—a review, Metals 4 (2014) 65–83.
[44] D.K. Ammisetti, S.S.H. Kruthiventi, S. Vinjavarapu, N.N. Babu, J.R. Gandepudi, S. K. Battula, A review on reinforcements, fabrication methods, and mechanical and wear properties of titanium metal matrix composites, J. Eng. Appl. Sci. 71 (2024) 60 (Article).
[45] A. Bartkowska, P. Bazarnik, Y. Huang, M. Lewandowska, T.G. Langdon, Using high-pressure torsion to fabricate an Al–Ti hybrid system with exceptional mechanical properties, Mater. Sci. Eng. A 799 (2021) 140114 (Article).
[46] M. Kawasaki, S.N. Alhajeri, C. Xu, T.G. Langdon, The development of hardness homogeneity in pure aluminum and aluminum alloy disks processed by high-pressure torsion, Mater. Sci. Eng. A 529 (2011) 345–351.
[47] X. Gao, D. Ai, J. Zhang, H. Yue, X. Zhang, C. Zhang, Z. Zhang, J. Chang, Interfacial structure and strengthening mechanisms of NiO-coated graphene reinforced aluminum matrix composites, J. Mater. Res. Technol. 35 (2025) 1494–1503.
[48] R. Guan, Y. Wang, S. Zheng, N. Su, Z. Ji, Z. Liu, Y. An, B. Chen, Fabrication of aluminum matrix composites reinforced with Ni-coated graphene nanosheets, Mater. Sci. Eng. A 754 (2019) 437–446.
[49] Z. Zheng, B. Nie, D. Chen, H. Sun, B. Shi, H. Qi, X. Li, X. Zhou, Improved reinforcing efficiency of reduced graphene oxide in aluminum matrix composites produced through flake self-assembly methods, Mater. Today Commun. 43 (2025) 111788 (Article).
[50] A. Mahato, S. Mondal, Fabrication and microstructure of micro and nano silicon carbide reinforced copper metal matrix composites/nanocomposites, Silicon 13 (2021) 1097–1105.
[51] S.S. Shankar, R.M. Shereema, R.B. Rakhi, Electrochemical determination of adrenaline using MXene/graphite composite paste electrodes, ACS Appl. Mater. Interfaces 10 (2018) 43343–43351.
[52] K. Allen-Perry, W. Straka, D. Keith, S. Han, L. Reynolds, B. Gautam, D.E. Autrey, Tuning the magnetic properties of two-dimensional MXenes by chemical etching, Materials 14 (2021) 694 (Article).
[53] H. Yun, Y. Chae, E. Kim, H.K. Kim, S. Jang, M.-H. Baik, C.W. Ahn, Y. Lee, Ultra-stable titanium carbide mxene functionalized with heterocyclic aromatic amines, Adv. Funct. Mater. 32 (2022) 2203296 (Article).
[54] H. Zheng, F. Wang, W. Si, Decorating Ti_3C_2 MXene nanosheets with Fe-N_x-C nanoparticles for efficient oxygen reduction reaction, Inorganics 13 (2025) 188 (Article).
[55] S. Varshney, M. Oded, S. Remennik, V. Gutkin, U. Banin, Controlling the surface of aluminum nanocrystals: from aluminum oxide to aluminum fluoride, Small 19 (2023) 2304478 (Article).
[56] P. Bindu, S. Thomas, Estimation of lattice strain in ZnO nanoparticles: X-ray peak profile analysis, J. Theor. Appl. Phys. 8 (2014) 123–134.
[57] A.R. Bushroa, R.G. Rahbari, H.H. Masjuki, M.R. Muhamad, Approximation of crystallite size and microstrain via XRD line broadening analysis in TiSiN thin films, Vacuum 86 (2012) 1107–1112.
[58] Z. Li, H. Ding, Y. Huang, T.G. Langdon, An evaluation of the mechanical properties, microstructures, and strengthening mechanisms of pure Mg processed by high-pressure torsion at different temperatures, Adv. Eng. Mater. 24 (2022) 2200799 (Article).
[59] F.A. Mohamed, S.S. Dheda, On the minimum grain size obtainable by high-pressure torsion, Mater. Sci. Eng. A 558 (2012) 59–63.
[60] M. Khajouei-Nezhad, M.H. Paydar, R. Ebrahimi, P. Jenei, P. Nagy, J. Gubicza, Microstructure and mechanical properties of ultrafine-grained aluminum consolidated by high-pressure torsion, Mater. Sci. Eng. A 682 (2017) 501–508.
[61] A. Roh, H.Y. Um, D. Kim, S. Nam, H.S. Kim, H. Choi, Influence of high-pressure torsion and hot rolling on the microstructure and mechanical properties of aluminum–fullerene composites, J. Mater. Sci. 52 (2017) 11988–12000.